Appendix C

Supplementary Information for Chapter 4: Protonation-induced chirality drives separation by DMS

This appendix contains the supporting information for Chapter 4, and is analogous to the supporting information to the following manuscript:
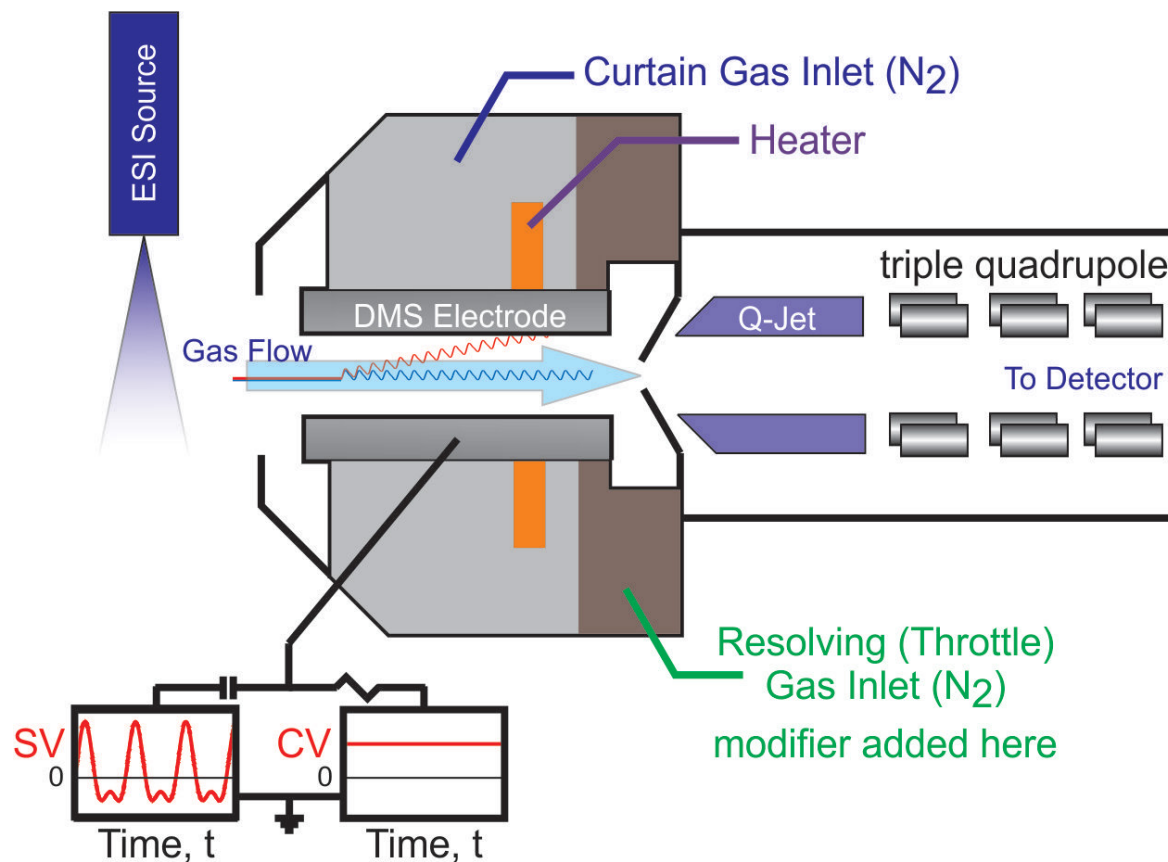
Ieritano, C., Le Blanc, J. C. Y., Schneider, B. B., Bissonnette, J. R., Haack, A., Hopkins, W. S. Protonation-Induced Chirality Drives Separation by Differential Ion Mobility Spectrometry. *Angew. Chem. Int. Ed.* **2022**. 61 (9), e202116794. *Frontispiece.*

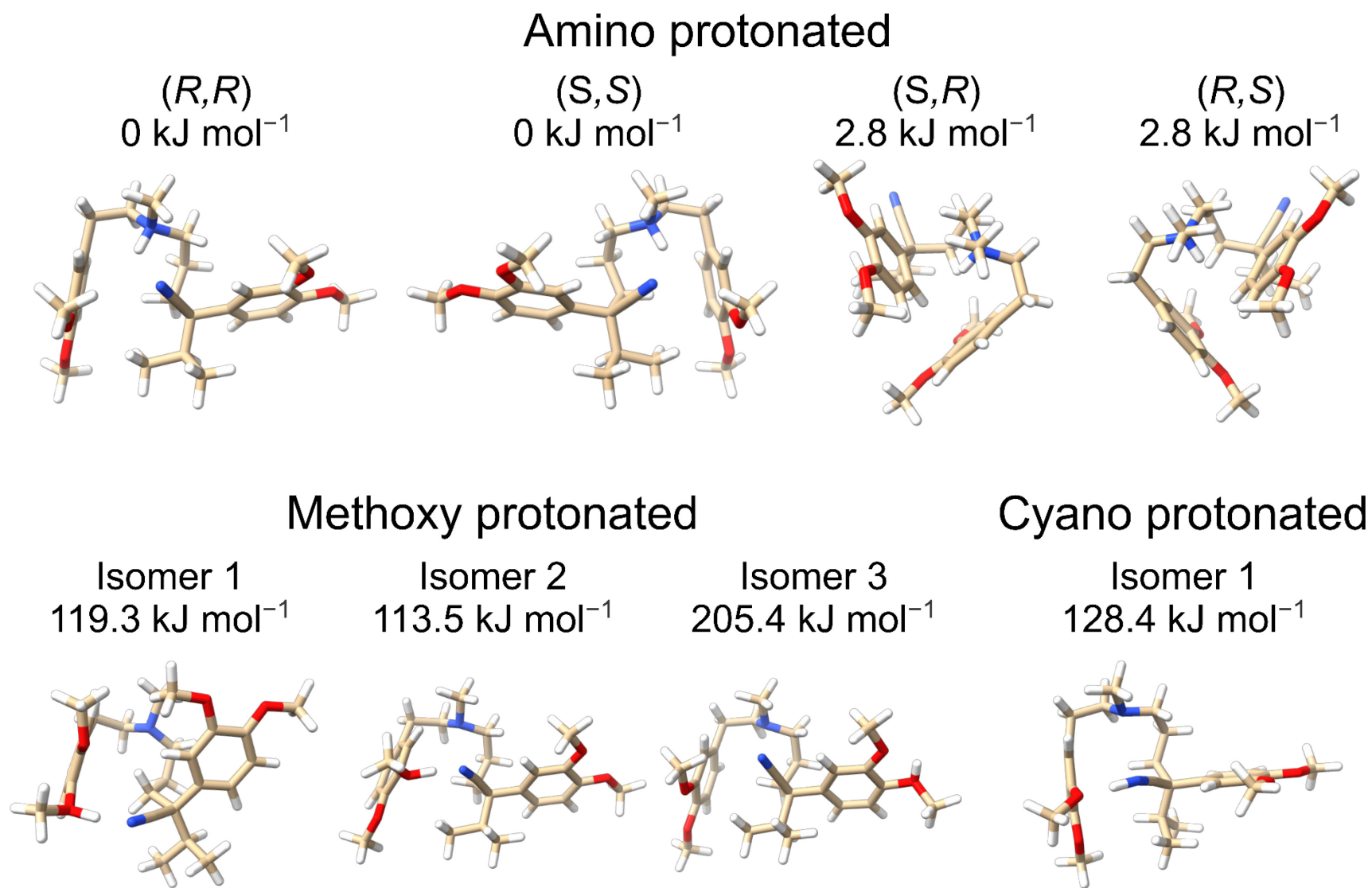https://onlinelibrary.wiley.com/doi/full/10.1002/anie.202116794

Table of Contents

Supporting Figures

Figure S4-1. The basic layout of a differential mobility spectrometry (DMS) cell consists of two-planar electrodes separated by a 1 mm gap. Ions are introduced to the DMS cell by ESI and carried through the device with the flow of the N_2 carrier gas (blue arrow). Application of the oscillating separation field, denoted the separation voltage (SV), induces off-axis motion (red trace) of the analytes that is determined by their field dependent mobility. Ion trajectories are stabilized by application of a static direct-current compensation voltage (CV) such that they elute from the DMS cell to the mass spectrometer (blue trace). The magnitude of the CV applied is correlated with the differential mobility of the ion, enabling spatial resolution of analytes as they are directed towards the exit orifice of the DMS cell to the mass spectrometer.

V126300

V126305

D461275
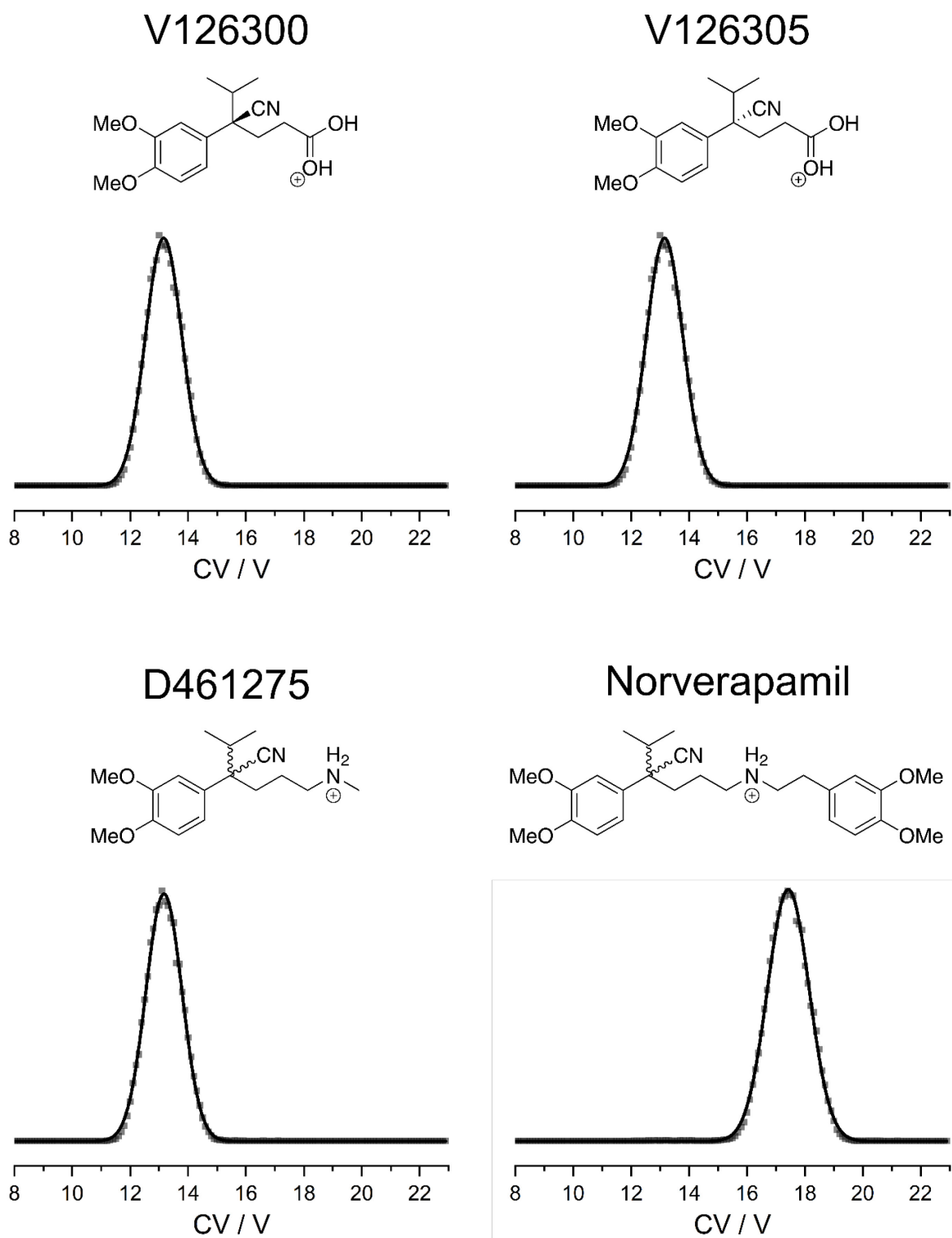
Norverapamil

Figure S4-2. DMS behaviour of protonated verapamil metabolites and analogs exhibit a singular peak in the DMS ionogram. Compound structures are shown below their Toronto Research Chemicals catalog number. Ionograms are obtained at SV = 4500 V with the bath gas heater set to 150 °C and with the resolving gas on (N_2; 10 psi). Data points (transparent squares) are fit to a single Gaussians (black line).

4

Amino protonated

(R,R)
0 kJ mol^{-1}

(S,S)
0 kJ mol^{-1}

(S,R)
2.8 kJ mol^{-1}

(R,S)
2.8 kJ mol^{-1}

Methoxy protonated

Cyano protonated

Isomer 1
119.3 kJ mol^{-1}

Isomer 2
113.5 kJ mol^{-1}

Isomer 3
### 205.4 kJ mol^{-1}

Isomer 1
128.4 kJ mol^{-1}

Figure S4-3. Prototropic isomers of (R)-verapamil. Standard Gibbs energies are calculated at the ωB97X-D/Def2-TZVP level of theory (see Supporting Section S4-3) and reported relative to the lowest energy protonation site (the tertiary amine).
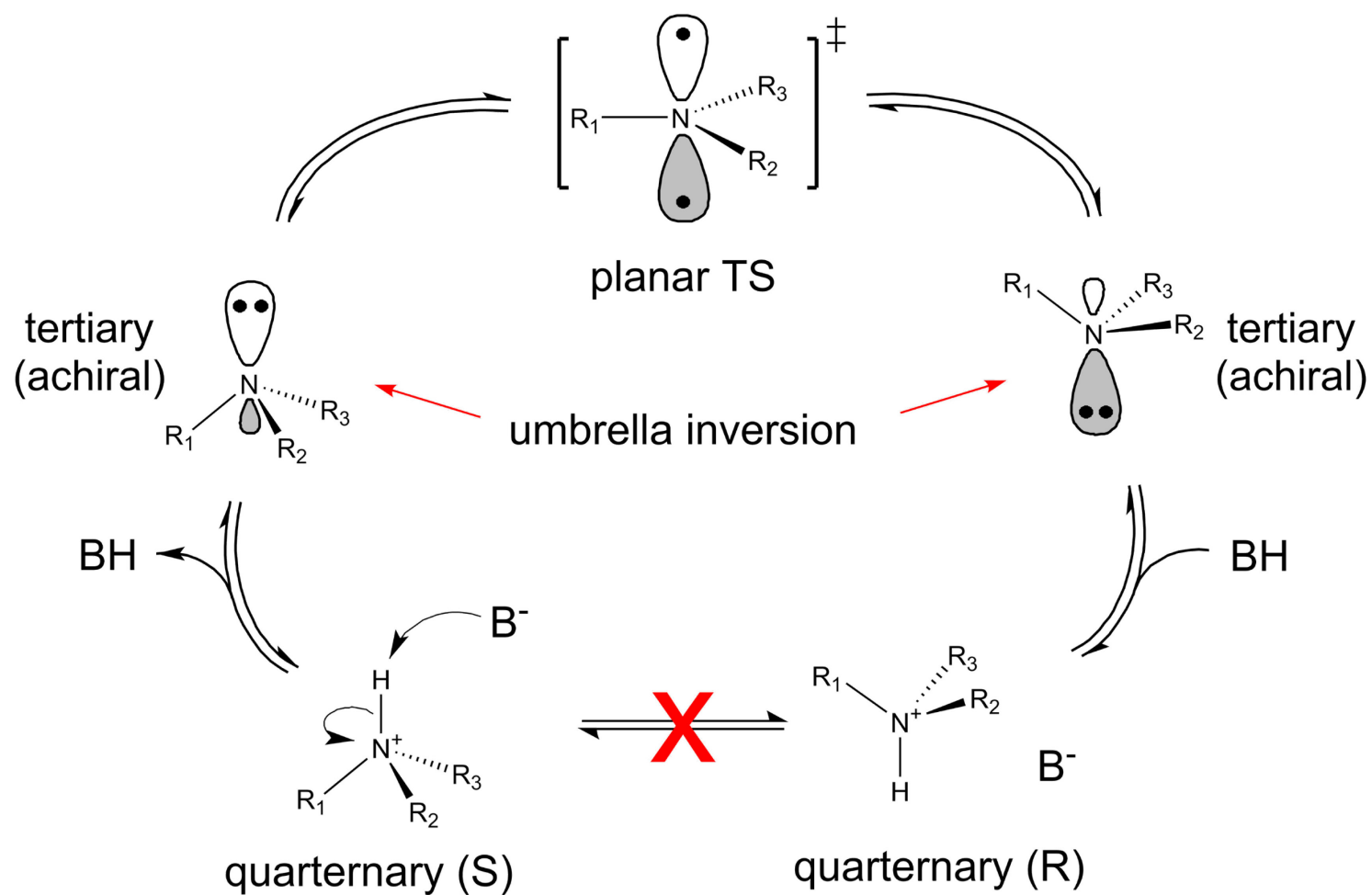
Figure S4-4. An overview of nitrogen inversion in tertiary amines, whereby a dynamic, solution-phase equilibrium exists between the neutral (tertiary) and protonated (quaternary) species. Solvent-mediated (B⁻) proton abstraction from the protonated, quaternary amine enables nitrogen inversion to take place on the tertiary species via a trigonal planar transition state. However, the protonated, quaternary amine cannot directly invert to the opposite stereochemical configuration; it must first be deprotonated by a sufficiently basic ligand to generate the tertiary species. Due to this solution-phase equilibrium, tertiary amines are achiral (even when protonated). After protonation of a tertiary amine during the ESI process and removal of solvent, the resulting quaternary amine can no longer convert back into the tertiary species and generates a new chiral centre.

Verapamil dispersion curves
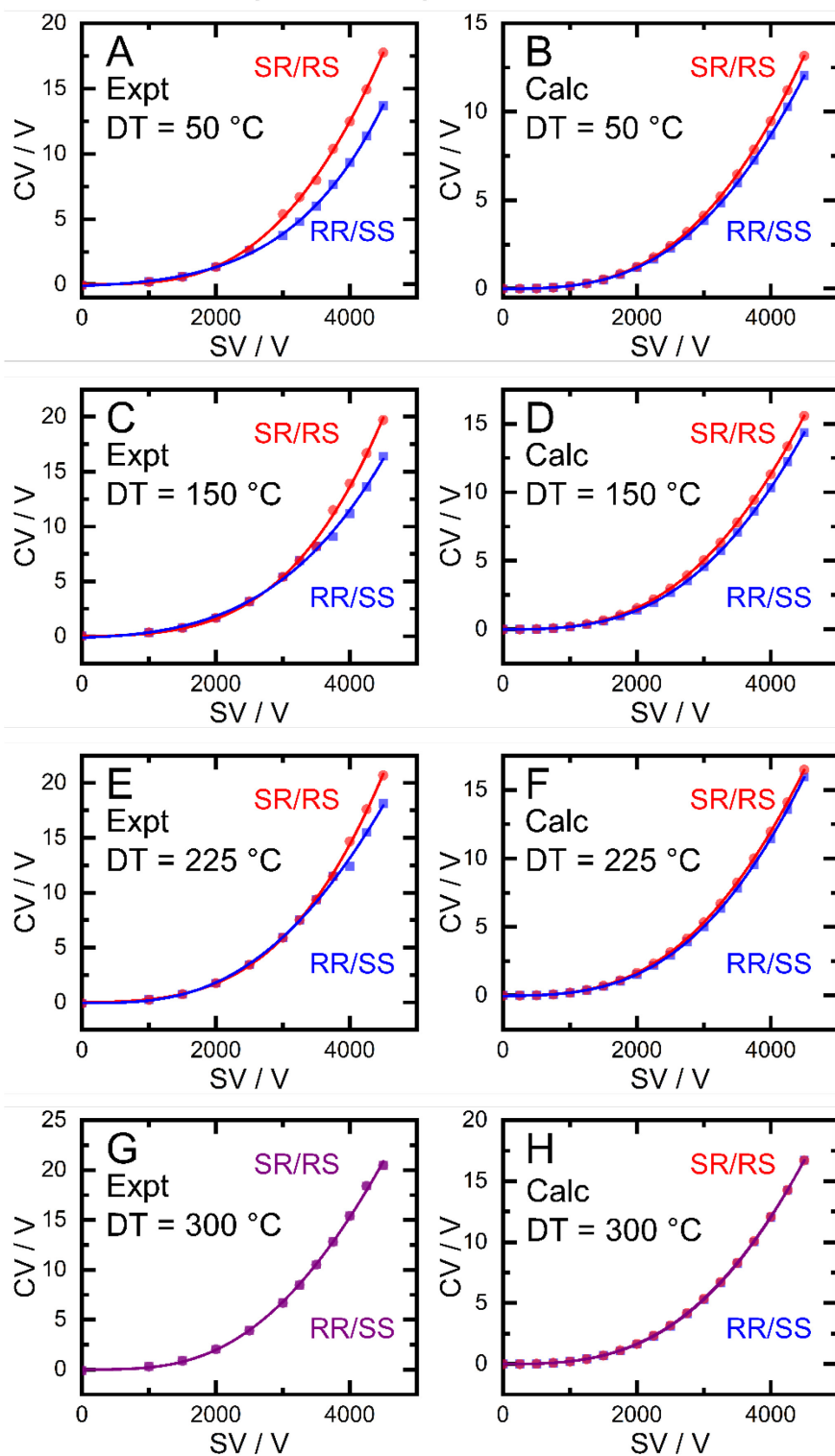
Figure S4-5. Dispersion curves of verapamil obtained experimentally and via *in silico* modelling at bath gas temperature settings of 50 °C (**A** and **B**, respectively), 150 °C (**C** and **D**, respectively), 225 °C (**E** and **F**, respectively), and 300 °C (**G** and **H**, respectively).
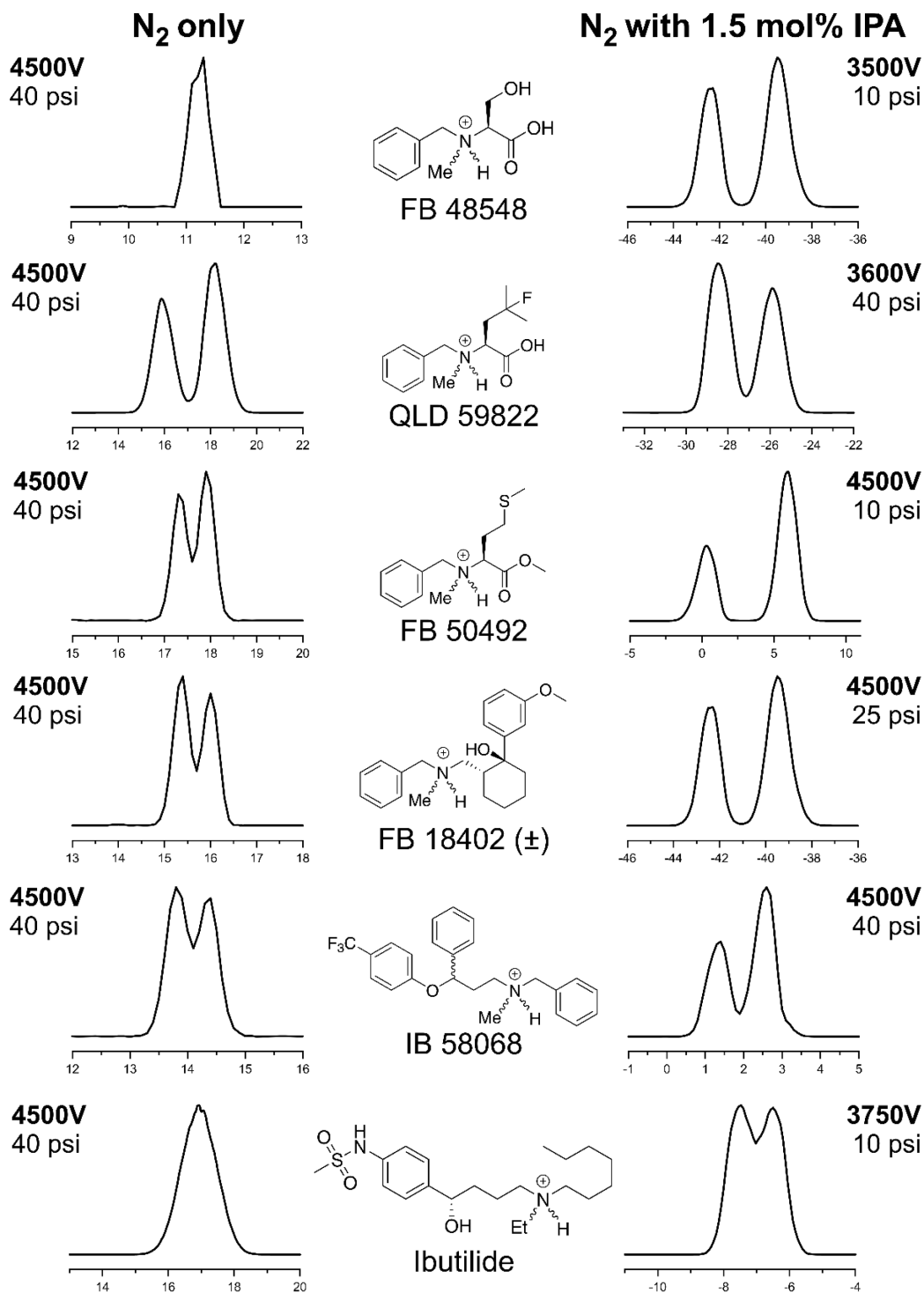
Norverapamil dispersion curves
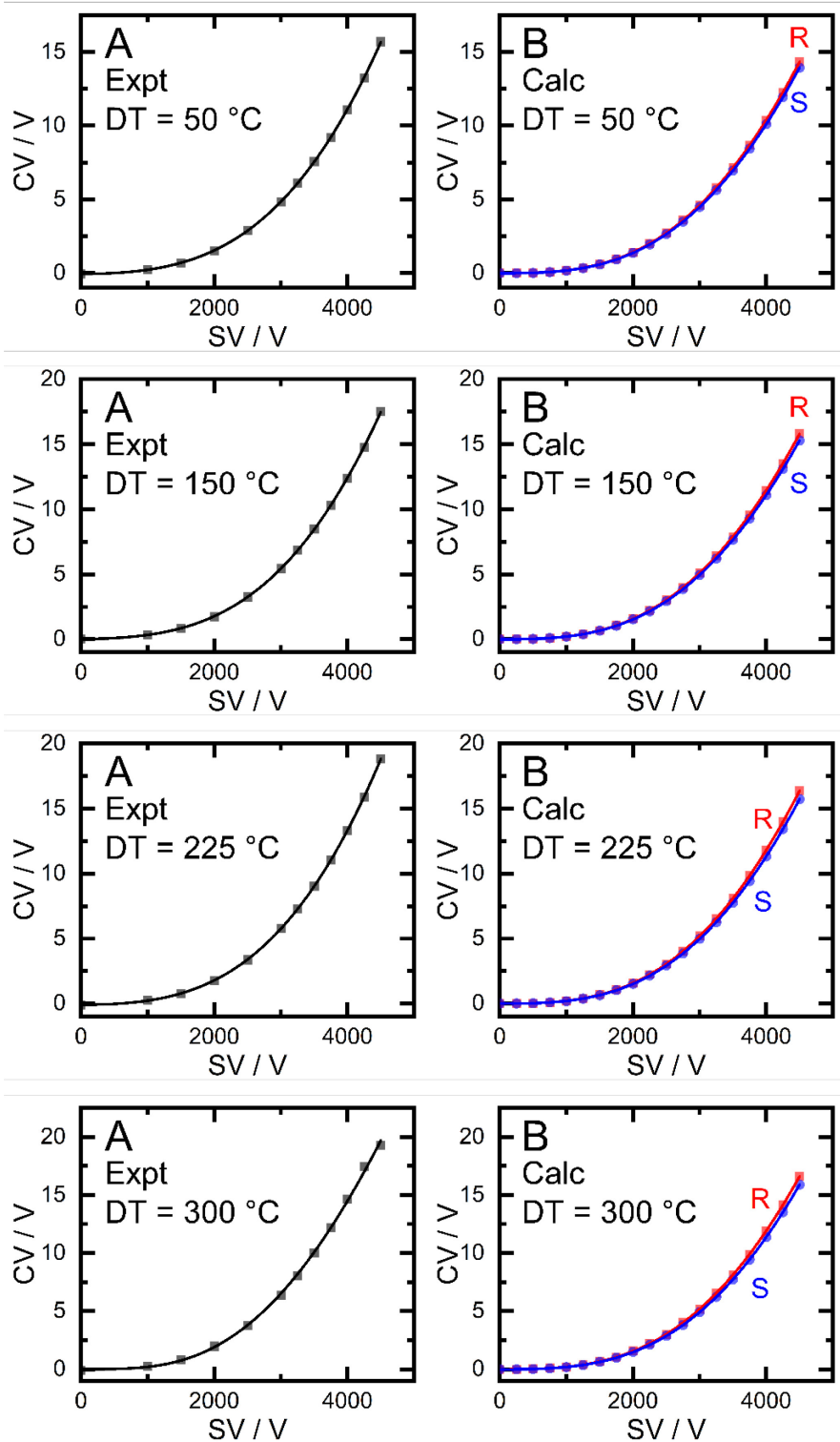
Figure S4-6. Dispersion curves of norverapamil obtained experimentally and via *in silico* modelling at bath gas temperature settings of 50 °C (**A** and **B**, respectively), 150 °C (**C** and **D**, respectively), 225 °C (**E** and **F**, respectively), and 300 °C (**G** and **H**, respectively).

8

Figure S4-7. Experimental ionograms plots of 6 molecules dissimilar from verapamil. Ionograms in the left pane were acquired in a pure N_2 DMS environment, whereas ionograms on the right panel were acquired and an N_2 environment that was seeded with 1.5 mol% of isopropanol (IPA). In general, seeding the DMS carrier gas with volatile chemical modifiers improves the separation. SVs and resolving gas pressures are provided at the top of each ionogram. Apart from Ibutilide, compound names are given as their Carbosynth catalog number.

N₂ only

4500V
25 psi

13 15 17 19 21 23

4500V
25 psi

12 14 16 18 20 22

4500V
25 psi

10 12 14 16 18 20

(±)-Verapamil Impurity H

(±)-O-desmethyl Verapamil

(±)-Anipamil

N₂ with 1.5 mol% IPA

4500V
25 psi

-7 -5 -3 -1 1 3 5 7 9

4400V
40 psi

-9 -7 -5 -3 -1 1 3 5 7 9

4500V
10 psi

-10 -5 0 5 10
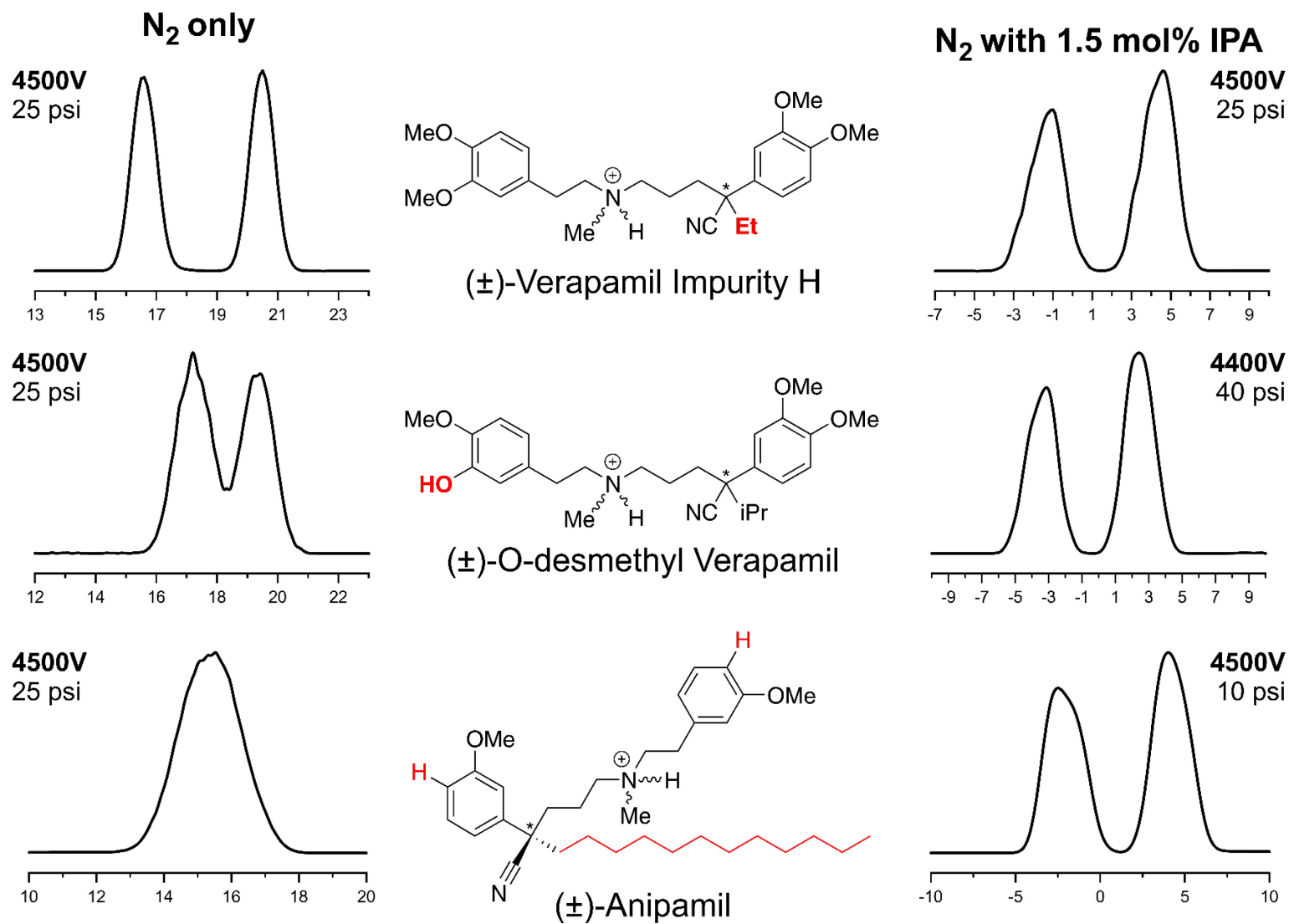
Figure S4-8. Experimental ionograms plots of 3 verapamil-like molecules dissimilar from verapamil. Structural differences from verapamil are shown in red. Ionograms in the left pane were acquired in a pure N₂ DMS environment, whereas ionograms on the right panel were acquired and an N₂ environment that was seeded with 1.5 mol% of isopropanol (IPA). In general, seeding the DMS carrier gas with volatile chemical modifiers improves the separation. SVs and resolving gas pressures are provided at the top of each ionogram.

Supplementary Sections

Section S4-1: Experimental details pertaining to Differential Mobility Spectrometry (DMS)

A planar SelexION differential mobility spectrometer with a 1 mm gap between the electrodes (SCIEX, Canada) was mounted in the atmospheric region between the sampling orifice of a QTRAP 5500 hybrid triple quadrupole linear ion trap mass spectrometer and a Turbospray electrospray ionization (ESI) source (SCIEX). This instrumental setup has been described extensively in the literature and is shown in Figure S4-9.[1–3]
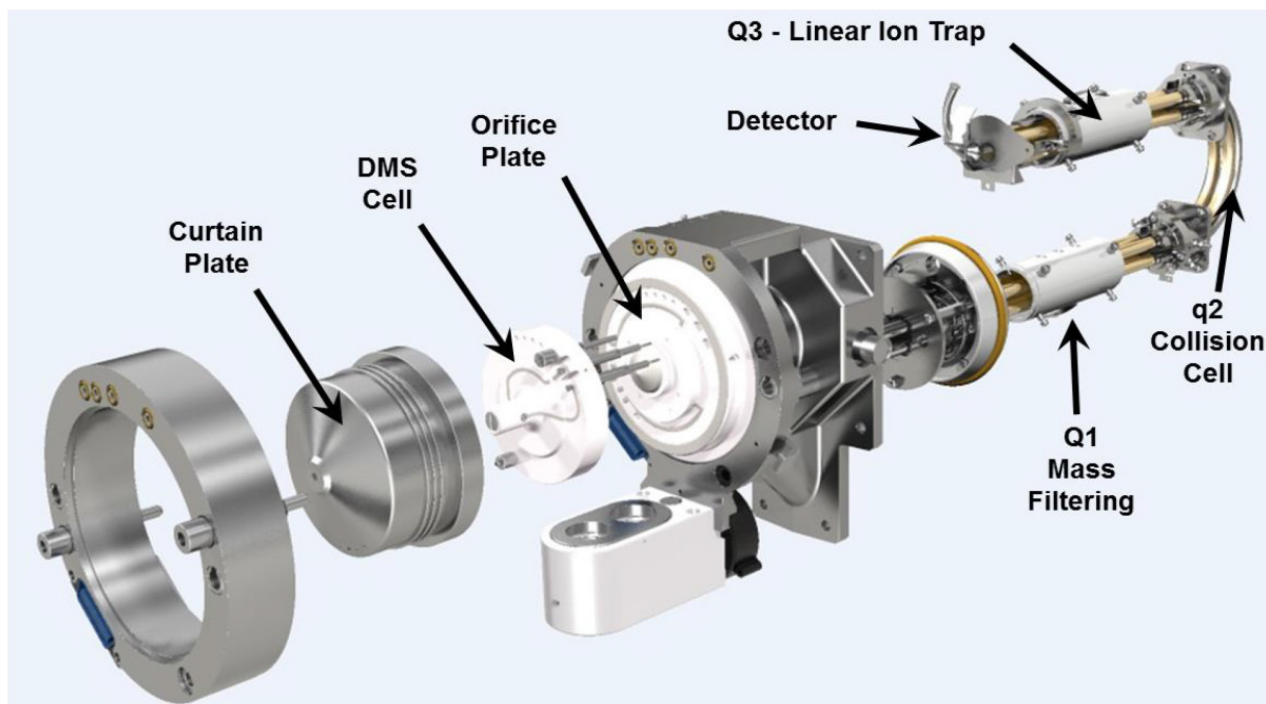
Figure S4-9. Schematic of the SELEXION system coupled to the QTRAP 5500 (SCIEX) hybrid linear ion trap triple-quadrupole mass spectrometer. The QJet region shown in Figure S1 is not labelled but exists between the orifice plate and Q1.

All data acquisition was acquired by direct infusion of the analyte mixture into the ESI source. All chemicals were purchased from Toronto Research Chemicals, Sigma Aldrich, or Carbosynth and solubilized in 50:50 MeOH:H_2O (0.1% formic acid). Analyte mixtures contained 100 ng · mL^{-1} of

each species and were infused into the ESI source operating in positive mode at a flow rate of 10 µL min^{-1}. The ESI probe was set to 5500 V and ambient temperature. A nebulizing gas pressure of 30 psi and an auxiliary gas pressure of 10 psi was introduced to the ESI source to aid in desolvation. N$_2$ was used as source gas, the curtain gas in the DMS cell (20 psi), the throttle gas (10 psi), and as the collision gas in q2 (*ca.* 7 mTorr) for data acquisition in multiple reaction monitoring (MRM) mode. The following settings were employed in Analyst 1.7 for the ion optics: entrance potential (EP) of 10 V, collision cell exit potential (CXP) of 15 V, declustering potential (DP) of 100 V, DMS offset potential (DMO) of −3 V, and a collision gas (CAD) setting of low. A summary of all instrumental parameters used is provided in Table S4-1 on the following page.

DMS experiments to map ion differential mobility were conducted at 50 °C, 150 °C, 225 °C, or 300 °C. Note that these heater settings corresponded to effective bath gas temperature of 30 °C, 100 °C, 150 °C, and 177 °C, respectively.[4,5] DMS measurements consisted of stepping the SV from 0 V to 3000 V in 500 V increments and in 250 V increments thereafter up to SV = 4500 V. At each SV, the ion current was monitored as the CV was scanned from −10 V to 30 V in increments of 0.1 V to produce an ionogram. Each ionogram is fit with a Gaussian distribution, for which the centroid was taken as the CV that corresponds to maximum ion transmission. The CV required for maximum ion transmission at a particular SV was recorded for each ion. Dispersion plots are generated by fitting the SV/CV data to the inverse Maxwell-Boltzmann function shown in Equation S1, where *a*, *b*, *c*, and *d* are fit parameters.

$$CV = \left(\frac{1}{d}\right)\left(1 - \left[(a - SV)\exp\left(-\frac{(a - SV)}{b + ((c)(SV))}\right)\right]\right) \tag{S1}$$

Table S4-1. Operating conditions of the ESI-DMS-QTRAP5500.

Parameter	Setting
Source	
Curtain Gas (CUR)	20.0
Ion spray voltage (IS)	5500
Source Temperature (TEM)	50
Nebulizing Gas Pressure (GS1)	30.0
Auxiliary Gas Pressure (GS2)	10.0
Compound	
Declustering Potential (DP)	100
Entrance Potential (EP)	10
Collision Energy (CE)	Varies
Collision Cell Exit Potential (CXP)	15
DMS	
DMS Temperature (DT)	50, 150, 225, 300
Modifier (MD)	None
Separation Voltage (SV)	Varies
Compensation Voltage	Varies
DMS Offset (DMO)	-3.0
DMS Resolution Enhancement (DR)	Off
Resolution – Quad 1	
Ion Energy 1 (IE1)	1.1
Q1 Resolution	Unit
Resolution – Quad 3	
Ion Energy 3 (IE3)	1.8
Q3 Resolution	Unit
Detector	
CEM (CEM)	2100.0

Section S4-2: Experimental details pertaining to travelling-wave ion mobility spectrometry (TWIMS) Experiments and Calibration of Collision Cross Sections (CCSs)

A series of calibrant ions were purchased from Sigma Aldrich (Oakville, ON, Canada) and used without further purification (see Table S2 on the following page). The calibrant ions were solubilized in 50:50 H_2O:MeCN (with 0.1% formic acid) such that the concentration of each sample was $100 \ ng \cdot mL^{-1}$. Ionization was performed by direct infusion of the solution into the sample sprayer port of a standard electrospray ionization (ESI) source equipped to a Synapt G2Si system (Waters Corp.). Conversion of drift times to CCSs was performed using an established protocol.[6] Briefly, CCSs for calibrant ions, as measured by drift-tube IMS,[7] were adjusted to *CCS'* using Equation S2,

$$CCS' = \frac{(CCS)\sqrt{\mu}}{z} \tag{S2}$$

where μ is the reduced mass of the ion and buffer gas (N_2) and z is the charge of the ion. Transformation of the CCS to CCS' gives direct proportionality to the ion's inverse mobility as per the Mason-Schamp relationship.[8]

The arrival time distributions of each calibrant ion was fit with a Gaussian distribution (Equation S3), where y_0 is the base, A is the area, w is the full-width half-max, and x_c is the centroid of the peak.

$$y = y_0 + \frac{A \left(\exp \left(\frac{-(4\ln(2))(x - x_c)^2}{w^2} \right) \right)}{w \left(\sqrt{\frac{\pi}{4\ln(2)}} \right)} \tag{S3}$$

The centroid of each Gaussian was taken as the ion's arrival time (t_A), which was corrected for its mass-dependent flight time (t') between the TWIMS cell and the ToF analyzer (Equation S4).

$$t' = t_A - \left[\left(\frac{c}{1000} \right) \left(\sqrt{\frac{m}{z}} \right) \right] \tag{S4}$$

The constant c is dependent on the voltages used in the transfer optics (the Enhanced Duty Cycle (EDC) delay coefficient, which is 1.35 in this case). *CCS'* values were plotted against *t'* (in

milliseconds) and fit to the power function described in Equation S5, where a and n are fit parameters. This plot is shown in Figure S4-10 for ion mobility analyses performed using travelling wave velocities of 2500 and 2000 m · s^{-1} (wave height of 40 V), as well as 1500 m · s^{-1} at a wave height of 30 V.

$$CCS' = a(t')^n \tag{S5}$$

A summary t_A, t', CCS, and CCS' for each calibrant ion is provided in Table S4-2. CCSs of verapamil and norverapamil were determined by evaluating CCS' (Equation S5) from t' (Equation S4). CCS' is then used to evaluate CCS as per Equation S2. A summary of the CCSs determined for verapamil and norverapamil is shown in Table S4-3.
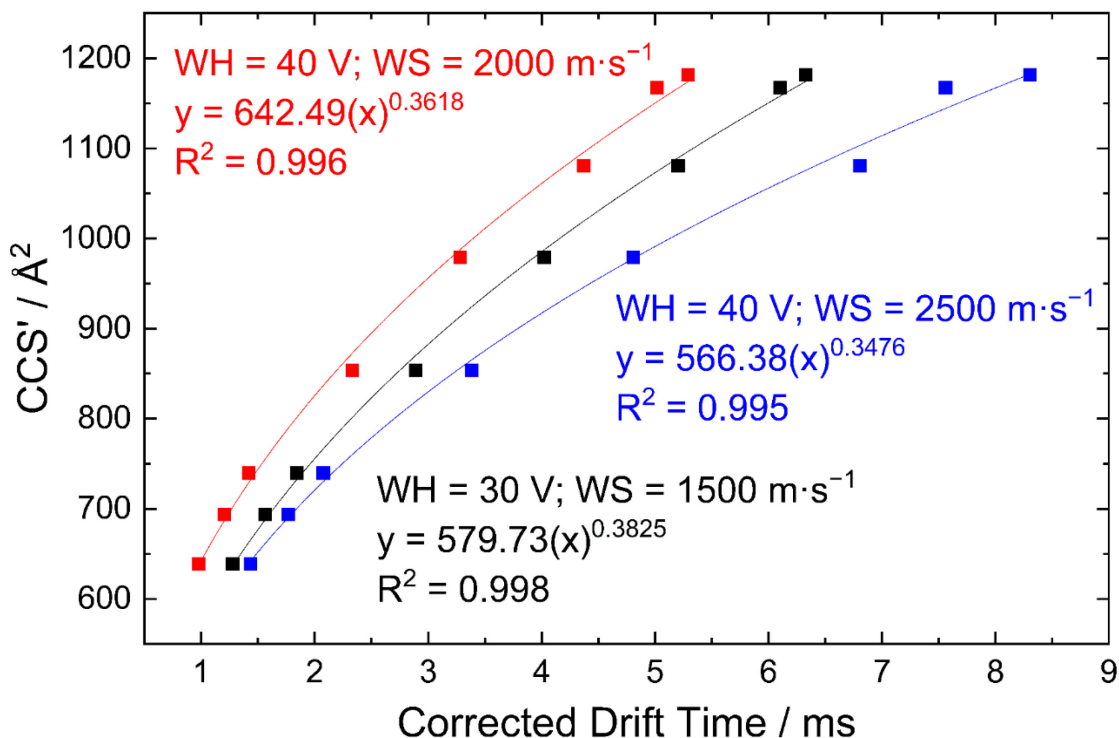
Figure S4-10. TWIMS calibration using a set of small molecule calibrant ions. A power function ($y = Ax^n$) was fit to the data, where A and n are fit parameters. Data was acquired at travelling wave velocities and amplitudes of 2500 m · s^{-1} and 40 V (blue), 2000 m · s^{-1} and 40 V (red), and 1500 m · s^{-1} and 30 V (black), respectively.

Table S4-2. *m/z*, CCS, and arrival times of the small molecule calibrant ions. Drift tube CCS values were obtained from reference 7 and converted to CCS' values using equation S2. Arrival times (t_A) for the calibrant ions were determined at travelling wave velocities and amplitudes of 2500 m·s⁻¹ and 40 V (blue), 2000 m·s⁻¹ and 40 V (red), and 1500 m·s⁻¹ and 30 V (black), respectively. Only the wave speed is reported in the table. Arrival times are corrected for their mass dependent drift times (t') as per Equation S4.

Compound	m/z	CCS / Å²	CCS' / Å²	Wave speed / m·s⁻¹	t_A / ms	FWHM / ms	t' / ms
Acetaminophen	152.0712	131.4	639.02	1500	1.29	0.27	1.27
				2000	0.99	0.23	0.98
				2500	1.45	0.26	1.43
Caffeine	195.0882	140.2	693.82	1500	1.58	0.28	1.56
				2000	1.22	0.25	1.20
				2500	1.78	0.28	1.77
Sulfaguanidine	215.0603	148.6	739.71	1500	1.86	0.26	1.84
				2000	1.44	0.23	1.42
				2500	2.10	0.28	2.08
Sulfadiamethoxine	311.0804	168.4	853.59	1500	2.91	0.32	2.89
				2000	2.35	0.28	2.33
				2500	3.41	0.38	3.38
Val-Tyr-Val	380.2185	191.7	979.07	1500	4.05	0.35	4.02
				2000	3.31	0.29	3.28
				2500	4.83	0.48	4.81
Terfenadine	472.3216	227.0	1167.20	1500	6.13	0.47	6.10
				2000	5.05	0.28	5.02
				2500	7.59	0.79	7.56
(DL-alanine)₇	516.2782	209.7	1080.82	1500	5.23	0.50	5.20
				2000	4.40	0.41	4.37
				2500	6.84	0.75	6.81
Leucine-Enkephalin	556.2771	228.8	1181.45	1500	6.35	0.47	6.32
				2000	5.32	0.40	5.29
				2500	8.34	0.94	8.30

Table S4-3. Drift time and full-width half-max of the ATD of verapamil and norverapamil determined at travelling wave velocities and amplitudes of 2500 m · s⁻¹ and 40 V, 2000 m · s⁻¹ and 40 V, and 1500 m · s⁻¹ and 30 V, respectively.

		Wave Speed		
Compound	**Parameter**	**1500** $\mathrm{m \cdot s^{-1}}$	**2000** $\mathrm{m \cdot s^{-1}}$	**2500** $\mathrm{m \cdot s^{-1}}$
Verapamil (Single Gaussian Fit) *m/z* 455.2910	t_A / ms	5.13	4.27	6.46
	ATD FWHM / ms	0.58	0.48	0.81
	t' / ms	5.11	4.24	6.43
	CCS' / Å²	1080.18	1081.95	1081.26
	CCS / Å²	210.30	210.64	210.51
	Average CCS = 210.48 ± 0.17 Å²			
Norverapamil *m/z* 441.2675	t_A / ms	4.92	4.07	6.07
	ATD FWHM / ms	0.52	0.43	0.71
	t' / ms	4.89	4.04	6.05
	CCS' / Å²	1062.42	1063.60	1058.33
	CCS / Å²	207.02	207.26	206.23
	Average CCS = 206.84 ± 0.54 Å²			
Verapamil (Double Gaussian Fit; left peak) *m/z* 455.2910	t_A / ms	5.05	4.20	6.28
	ATD FWHM / ms	0.52	0.43	0.71
	t' / ms	5.02	4.17	6.25
	CCS' / Å²	1073.38	1075.26	1070.35
	CCS / Å²	208.97	209.34	208.38
	Average CCS = 208.90 ± 0.48 Å²			
Verapamil (Double Gaussian Fit; right peak) *m/z* 455.2910	t_A / ms	5.26	4.37	6.60
	ATD FWHM / ms	0.52	0.43	0.71
	t' / ms	5.23	4.34	6.57
	CCS' / Å²	1089.82	1090.96	1088.94
	CCS / Å²	212.17	212.39	212.00
	Average CCS = 212.19 ± 0.20 Å²			

Section S4-3: Details of the Basin-Hopping, Density Functional Theory, and CCS Calculations

The potential energy surface (PES) of each stereochemical configuration of N-protonated verapamil [(R,R), (S,S), (R,S), and (S,R)] and N-protonated norverapamil [(R) and (S)] was mapped using a custom-written basin-hopping (BH) algorithm interfaced with Gaussian 16 (Version C.01).[9] Note that N-protonation refers to protonation on the amino moiety. For BH searches,[10–14] ions were modelled with the Universal Force Field (UFF),[15] which used partial charges for a 'guess structure' calculated at the ωB97X-D/Def2-TZVP level of theory[16–18] according to the Merz–Singh–Kollman (MK) partition scheme.[19,20] At each step of the BH algorithm, all rotatable dihedral angles were randomly distorted by $-10° \leq \Phi \leq 10°$. In total, 20000 structures were sampled for each stereoisomer. Typically, the BH routine would identify 100 – 300 low-energy conformers for each molecular cation. Candidate structures were then carried forward for pre-optimization at the semi-empirical PM7 level of theory[21,22] and subsequently sorted based on cosine similarities. For details on cosine similarities, see reference 23. Unique conformers within 75 kJ mol^{-1} of the PM7 global minimum were then treated at the ωB97X-D/Def2-TZVP level of theory. Partial charges were recalculated according to the MK partition scheme for later use in collision cross section (CCS) calculations. Normal mode analyses were also conducted to verify that each structure corresponded to a minimum on the PES and to estimate the gas-phase thermochemical quantities for each species (enthalpy, entropy, and Gibbs energy).

The MobCal-MPI code was used to calculate ion-neutral CCSs in N_2 using DFT optimized geometries and MK partial charges.[24,25] All CCS calculations involved 10 complete cycles of mobility calculations that used 48 points of velocity integration and 1024 points of impact parameter integration. Calculated CCSs values for a single isomer are reported as average values with standard deviations (< 1.7 Å^2) assessed from the 10 cycles of calculation. The CCS of each isomer was used to calculate the final Boltzmann-weighted CCS using the Gibbs corrected energies determined at the ωB97X-D/Def2-TZVPP level of theory. The temperature used in the Boltzmann-weighting scheme is the same as the temperature used in the trajectory method.

Section S4-4: Details of the *in silico* Dispersion Plot Modelling

Dispersion plots (*i.e.,* the CV necessary for optimal ion transmission at a given SV) are calculated using a self-consistent 2-temperature theory (SC2TT) approach as described in reference 4. Briefly, one starts with the assumption that all conformers are in thermal equilibrium with each other. The CCS of each conformer is then evaluated over a range of effective temperatures (T_{eff}) using MobCal-MPI.[24] CCSs are then fit to the empirical relationship shown in Equation S6 as a function of T_{eff}, where a, b and c are the fitting parameters.

$$CCS(T_{eff}) = a(T_{eff})^b + c \tag{S6}$$

The drift velocity (v_D) of each conformer is evaluated using Equation S7 at a specific field strength (E), gas number density (N), and bath gas temperature (T_{bath}). The ion's mobility (K) is treated with the Mason-Schamp equation[26,27]

$$v_D = KE = \left(\frac{3}{8}\right) \sqrt{\left(\frac{\pi}{2\mu k_B T_{eff}}\right)} \left(\frac{qE}{(N)\left(CCS(T_{eff})\right)}\right) \tag{S7}$$

where v_D is the drift velocity, M is the mass of the drift gas (N_2 in this case), μ is the reduced mass of the ion-neutral pair, k_B is the Boltzmann constant, and q is the ion's charge. The ion's mobility is then used to calculate its effective temperature as per equation S8, which follows the first approximation of two-temperature theory.[26,27]

$$T_{eff} = T_{bath} + \frac{M}{3k_B}(v_D)^2 \tag{S8}$$

With the ion's effective temperature in hand, K is revaluated using both the new effective temperature and the ion's CCS evaluated at the new effective temperature, which is updated from the fitting function (Equation S6). This process is completed iteratively until $\Delta T_{eff} < 10^{-4}$ K. Note that the first iteration assumes that $T_{eff} = T_{bath}$ and that T_{bath} is different from the temperature setting of the DMS heater. DMS heater settings of 50, 150, 225, and 300 °C correspond to bath gas temperatures of 30, 100, 150, and 177 °C, respectively.[5]

To increase the accuracy of this description, we used an extension to 2-temperature theory, which constitutes an approximation to the 2nd order mobility correction described by Siems *et al.*[28] Here,

the effective temperature and the mobility are corrected by the parameters α_{2T2} and β_{2T2} (Equations S9 and S10)

$$\alpha_{2T2} = \frac{-12\widehat{m}^3 - 16\widehat{m}^2 + 13\widehat{m}}{24\widehat{m}^3 + 32\widehat{m}^2 + 4\widehat{m} + 15} \tag{S9}$$

$$\beta_{2T2} = \frac{-3\widehat{m}^2 + 3\widehat{m}}{16\widehat{m}^2 - 6\widehat{m} + 5} \tag{S10}$$

where $\widehat{m} = m_{ion}/(m_{ion} + M)$. Implementing the correction factors into Equations S7 and S8 yield Equations S11 and S12, respectively.

$$v_D = KE = \left(\frac{3}{8}\right)\sqrt{\left(\frac{\pi}{2\mu k_B T_{eff}}\right)}\left(\frac{qE}{(N)\left(CCS(T_{eff})\right)}\right)(1 + \alpha_{2T2}K') \tag{S11}$$

$$T_{eff} = T_{bath} + \frac{M}{3k_B}(v_D)^2 \cdot (1 + \beta_{2T2}K') \tag{S12}$$

These values need to be multiplied by the field dependent quantity K', for which an approximation can be derived (Equation S13).[27]

$$K' \equiv \frac{d \ln(K)}{d \ln\left(\frac{E}{N}\right)} \approx -\frac{\widehat{C}}{\left(\frac{(T_{eff})}{(T_{eff} - T_{bath})}\right) + \widehat{C}} \tag{S13}$$

The dimensionless quantity $\widehat{C}$ can be expressed in terms of the CCS using Equation S14.[27]

$$\widehat{C} = 1 + 2\frac{d \ln(CCS)}{d \ln(T_{eff})} = 1 + \left(2\left(\frac{ab}{a + c \cdot (T_{eff})^{-b}}\right)\right) \tag{S14}$$

To obtain the right-hand-side, we used our fitting function from Equation S1 to determine the logarithmic derivative. The T_{eff} determined with and without the correction only differed by a few percent but yielded results closer to the experimental ones than using the original iteration scheme described in reference 4.

After the mobility of each cluster is obtained for range of field strengths, the mobility of the gas-phase ensemble (K_{ens}) is obtained by weighting the mobilities of the ith conformer in the ensemble (K_i) by its pseudo-thermal population, P_i (Equation S15). The reader is directed to reference 4 for the details of calculating P_i.

$$K_{ens} = \sum_i P_i \cdot K_i \qquad \text{(S15)}$$

K_{ens} is then used to predict a CV value for a given SV using Equation S16[29,30]

$$CV = -\frac{\langle \alpha\big(E_{SF}(t)\big) \cdot E_{SF}(t)\rangle_{wf}}{1 + \langle \alpha\big(E_{SF}(t)\big)\rangle_{wf} + \langle \alpha'\big(E_{SF}(t)\big) \cdot E_{SF}(t)\rangle_{wf}} \qquad \text{(S16)}$$

where $\alpha(E) = K_{ens}(E)/K_{ens}(0) - 1$ and $\alpha'(E)$ is its derivative with respect to E. The averages ($\langle...\rangle_{wf}$) are taken over one cycle of the waveform where $E_{SF}(t)$ is the time dependent separation field given by the asymmetric double sine function (Equation S17)

$$E_{SF}(t) = \frac{D}{d}\left(\frac{2}{3}\sin(\omega t) + \frac{1}{3}\sin\left(2\omega t - \frac{\pi}{2}\right)\right) \qquad \text{(S17)}$$

where D is the maximum amplitude of the waveform, which is equal to two-thirds of peak-to-peak SV (SV_{pp}) voltage ($D = 2/3 \cdot SV_{pp}$), d is the gap height between the DMS electrodes (1 mm), and ω is the oscillation frequency of waveform (3 MHz).

S4-5. Frequently Asked Questions

1. **Are amines always achiral in the solution phase?**

   In general, yes. However, a notable exception occurs when the protonation site of a chiral, quaternary amine intramolecularly coordinates with basic moieties of the molecule. Doing so would shield it from the solvation environment and would preserve the stereochemical configuration. This was observed in a study by MacGillvray and Atwood, whereby protonation of both amino moieties of Cryptand-222 yields one of three configurations: in-in, in-out, or out-out (https://pubs.acs.org/doi/10.1021/jo00121a007).
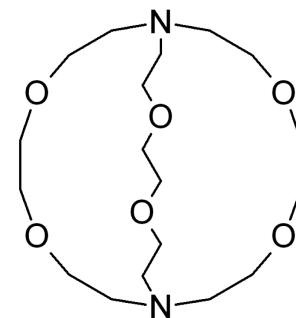
   Cryptand-222

   The evolution between these stereochemical configurations can be monitored by temperature dependent NMR in **aprotic** solvents (MeCN-d3, DMSO-d6). These results do show that tertiary amines can be chiral in the solution phase, but under very specific conditions. We searched the literature to see if this experiment has been performed in a protic NMR solvent (e.g., CD3OD). We could not find any, likely because 1) H/D exchange would make the amino protons invisible, and 2) rapid proton exchange with the NMR solvent would preclude the "freezing out" of a in-in, in-out, or out-out configuration (see Figure S4 of this manuscript).

2. **Can protonation-induced diastereomers of verapamil be resolved by liquid chromatography using a chiral column?**

   Unfortunately, the protonation induced chirality phenomenon would be very difficult to probe in the solution phase (even in an acidified solution). The rapid proton exchange occurring in the solution phase precludes formation of a permanent stereocenter at the tertiary amino moiety. As such, observation of protonation-induced chirality of amines in the solution phase will be unlikely unless the

protonation site is shielded from solvation (see discussion in the last paragraph of comment #3).

This fundamental caveat is compounded by the notorious difficulty associated with chiral LC; it often involves a lot of luck in finding the right mobile phase conditions and chiral column that suits the analyte of interest. That said, the enantiomeric forms of verapamil and norverapamil have been resolved by chiral LC previously (see https://doi.org/10.1093/chromsci/bms080). The authors of this study separate (R)-verapamil from (S)-verapamil, and (R)-norverapamil from (S)-norverapamil using an acidified acetonitrile/water gradient. No additional peaks corresponding to the protonation diastereomers are observed in the LC trace, likely due to the dynamic proton transfers that occur at the amino moiety in the solution phase.

References

(1)   Schneider, B. B.; Covey, T. R.; Coy, S. L.; Krylov, E. V.; Nazarov, E. G. Planar Differential Mobility Spectrometer as a Pre-Filter for Atmospheric Pressure Ionization Mass Spectrometry. *Int. J. Mass Spectrom.* **2010**, *298* (1–3), 45–54. https://doi.org/10.1016/j.ijms.2010.01.006.

(2)   Krylov, E. V.; Nazarov, E. G.; Miller, R. A. Differential Mobility Spectrometer: Model of Operation. *Int. J. Mass Spectrom.* **2007**, *266* (1–3), 76–85. https://doi.org/10.1016/j.ijms.2007.07.003.

(3)   Schneider, B. B.; Nazarov, E. G.; Londry, F.; Vouros, P.; Covey, T. R. Differential Mobility Spectrometry/Mass Spectrometry History, Theory, Design Optimization, Simulations, and Applications. *Mass Spectrom. Rev.* **2016**, *35* (6), 687–737. https://doi.org/10.1002/mas.21453.

(4)   Haack, A.; Crouse, J.; Schlüter, F. J.; Benter, T.; Hopkins, W. S. A First Principle Model of Differential Ion Mobility: The Effect of Ion-Solvent Clustering. *J. Am. Soc. Mass Spectrom.* **2019**, *30* (12), 2711–2725. https://doi.org/10.1007/s13361-019-02340-1.

(5)   Ieritano, C.; Featherstone, J.; Haack, A.; Guna, M.; Campbell, J. L.; Hopkins, W. S. How Hot Are Your Ions in Differential Mobility Spectrometry? *J. Am. Soc. Mass Spectrom.* **2020**, *31* (3), 582–593. https://doi.org/10.1021/jasms.9b00043.

(6)   Gabelica, V.; Shvartsburg, A. A.; Afonso, C.; Barran, P.; Benesch, J. L. P.; Bleiholder, C.; Bowers, M. T.; Bilbao, A.; Bush, M. F.; Campbell, J. L.; Campuzano, I. D. G.; Causon, T.; Clowers, B. H.; Creaser, C. S.; De Pauw, E.; Far, J.; Fernandez-Lima, F.; Fjeldsted, J. C.; Giles, K.; Groessl, M.; Hogan, C. J.; Hann, S.; Kim, H. I.; Kurulugama, R. T.; May, J. C.; McLean, J. A.; Pagel, K.; Richardson, K.; Ridgeway, M. E.; Rosu, F.; Sobott, F.; Thalassinos, K.; Valentine, S. J.; Wyttenbach, T. Recommendations for Reporting Ion Mobility Mass Spectrometry Measurements. *Mass Spectrom. Rev.* **2019**, *38* (3), 291–320. https://doi.org/10.1002/mas.21585.

(7)   Picache, J. A.; Rose, B. S.; Balinski, A.; Leaptrot, K. L.; Sherrod, S. D.; May, J. C.; McLean, J. A. Collision Cross Section Compendium to Annotate and Predict Multi-Omic Compound Identities. *Chem. Sci.* **2019**, *10* (4), 983–993. https://doi.org/10.1039/c8sc04396e.

(8)   Mason, E. A.; McDaniel, E. W. *Transport Properties of Ions in Gases*; John Wiley and Sons: New York, 1988.

(9)   Frisch, M. J.; Trucks, G. W.; Schlegel, H. B.; Scuseria, G. E.; Robb, M. A.; Cheeseman, J. R.; Scalmani, G.; V. Barone, B.; Mennucci, G.; Petersson, A. Gaussian 09. Gaussian Incorporated: Wallingford, CT 2009.

(10)   Wales, D. J.; Doye, J. P. K. Global Optimization by Basin-Hopping and the Lowest Energy

Structures of Lennard-Jones Clusters Containing up to 110 Atoms. *J. Phys. Chem. A* **1997**, *101* (28), 5111–5116. https://doi.org/10.1021/jp970984n.

(11)   Wales, D. *Energy Landscapes*; Cambridge University Press, 2004. https://doi.org/10.1017/cbo9780511721724.

(12)   Ieritano, C.; Featherstone, J.; Carr, P. J. J.; Marta, R. A.; Loire, E.; McMahon, T. B.; Hopkins, W. S. The Structures and Properties of Anionic Tryptophan Complexes. *Phys. Chem. Chem. Phys.* **2018**, *20* (41), 26532–26541. https://doi.org/10.1039/c8cp04533j.

(13)   Hopkins, W. S.; Marta, R. A.; McMahon, T. B. Proton-Bound 3-Cyanophenylalanine Trimethylamine Clusters: Isomer-Specific Fragmentation Pathways and Evidence of Gas-Phase Zwitterions. *J. Phys. Chem. A* **2013**, *117* (41), 10714–10718. https://doi.org/10.1021/jp407766j.

(14)   Scott Hopkins, W.; Marta, R. A.; Steinmetz, V.; McMahon, T. B. Mode-Specific Fragmentation of Amino Acid-Containing Clusters. *Phys. Chem. Chem. Phys.* **2015**, *17* (43), 28548–28555. https://doi.org/10.1039/c5cp03517a.

(15)   Rappé, A. K.; Casewit, C. J.; Colwell, K. S.; Goddard, W. A.; Skiff, W. M. UFF, a Full Periodic Table Force Field for Molecular Mechanics and Molecular Dynamics Simulations. *J. Am. Chem. Soc.* **1992**, *114* (25), 10024–10035. https://doi.org/10.1021/ja00051a040.

(16)   Chai, J. Da; Head-Gordon, M. Long-Range Corrected Hybrid Density Functionals with Damped Atom-Atom Dispersion Corrections. *Phys. Chem. Chem. Phys.* **2008**, *10* (44), 6615–6620. https://doi.org/10.1039/b810189b.

(17)   Weigend, F.; Ahlrichs, R. Balanced Basis Sets of Split Valence, Triple Zeta Valence and Quadruple Zeta Valence Quality for H to Rn: Design and Assessment of Accuracy. *Phys. Chem. Chem. Phys.* **2005**, *7* (18), 3297–3305. https://doi.org/10.1039/b508541a.

(18)   Grimme, S.; Antony, J.; Ehrlich, S.; Krieg, H. A Consistent and Accurate Ab Initio Parametrization of Density Functional Dispersion Correction (DFT-D) for the 94 Elements H-Pu. *J. Chem. Phys.* **2010**, *132* (15), 154104. https://doi.org/10.1063/1.3382344.

(19)   Besler, B. H.; Merz, K. M.; Kollman, P. A. Atomic Charges Derived from Semiempirical Methods. *J. Comput. Chem.* **1990**, *11* (4), 431–439. https://doi.org/10.1002/jcc.540110404.

(20)   Singh, U. C.; Kollman, P. A. An Approach to Computing Electrostatic Charges for Molecules. *J. Comput. Chem.* **1984**, *5* (2), 129–145. https://doi.org/10.1002/jcc.540050204.

(21)   Stewart, J. J. P. Optimization of Parameters for Semiempirical Methods VI: More Modifications to the NDDO Approximations and Re-Optimization of Parameters. *J. Mol. Model.* **2013**, *19* (1), 1–32. https://doi.org/10.1007/s00894-012-1667-x.

(22)   Throssel, K.; Frisch, M. J. Evaluation and Improvement of Semiempirical Methods I: PM7R8: A Variant of PM7 with Numerically Stable Hydrogen Bonding Corrections. *Manuscr. Prep.*

(23)   Zhou, C.; Ieritano, C.; Hopkins, W. S. Augmenting Basin-Hopping With Techniques From Unsupervised Machine Learning: Applications in Spectroscopy and Ion Mobility. *Front. Chem.* **2019**, *7*, 519. https://doi.org/10.3389/fchem.2019.00519.

(24)   Ieritano, C.; Crouse, J.; Campbell, J. L.; Hopkins, W. S. A Parallelized Molecular Collision Cross Section Package with Optimized Accuracy and Efficiency. *Analyst* **2019**, *144* (5), 1660–1670. https://doi.org/10.1039/c8an02150c.

(25)   Ieritano, C.; Hopkins, W. S. Assessing Collision Cross Section Calculations Using MobCal-MPI with a Variety of Commonly Used Computational Methods. *Mater. Today Commun.* **2021**, *27*, 102226. https://doi.org/10.1016/j.mtcomm.2021.102226.

(26)   Viehland, L. A.; Mason, E. A. Gaseous Lon Mobility in Electric Fields of Arbitrary Strength. *Ann. Phys. (N. Y).* **1975**, *91* (2), 499–533. https://doi.org/10.1016/0003-4916(75)90233-X.

(27)   Viehland, L. A.; Mason, E. A. Gaseous Ion Mobility and Diffusion in Electric Fields of Arbitrary Strength. *Ann. Phys. (N. Y).* **1978**, *110* (2), 287–328. https://doi.org/10.1016/0003-4916(78)90034-9.

(28)   Siems, W. F.; Viehland, L. A.; Hill, H. H. Correcting the Fundamental Ion Mobility Equation for Field Effects. *Analyst* **2016**, *141* (23), 6396–6407. https://doi.org/10.1039/c6an01353h.

(29)   Buryakov, I. A.; Krylov, E. V.; Nazarov, E. G.; Rasulev, U. K. A New Method of Separation of Multi-Atomic Ions by Mobility at Atmospheric Pressure Using a High-Frequency Amplitude-Asymmetric Strong Electric Field. *Int. J. Mass Spectrom. Ion Process.* **1993**, *128* (3), 143–148. https://doi.org/10.1016/0168-1176(93)87062-W.

(30)   Krylov, E. V.; Nazarov, E. G. Electric Field Dependence of the Ion Mobility. *Int. J. Mass Spectrom.* **2009**, *285* (3), 149–156. https://doi.org/10.1016/j.ijms.2009.05.009.